RESEARCH ARTICLE

A low-effort and inexpensive methodology to determine beam separation distance of multi-foci FLDI

Giannino Ponchio Camillo[1] · Alexander Wagner[1]

Abstract

A new method is presented to measure the separation distance between probing volumes of closely spaced multi-foci Focused Laser Differential Interferometers (FLDI). The accuracy and precision of this distance measurement directly translate into the quality of convection velocity measurements performed by means of arrays of FLDI. The suggested method is based on the detection of a propagating weak blast wave, generated with a simple and inexpensive apparatus using an automotive spark plug. Demonstration is conducted using an FLDI with two foci (D-FLDI). The generated blast wave is probed at multiple distances from its source to verify its weakening into an acoustic pulse, which offers ideal conditions to the proposed methodology. D-FLDI separation distance measurement using the new approach is compared to measurements using beam profiler images and to the alternative currently established in the literature, based on the FLDI response to a moving weak lens. Tests are made on varying internal configurations of the D-FLDI, while the distance between the two systems is kept constant. Results show the present method to have improved accuracy and robustness in comparison with the moving lens approach, while requiring significantly less effort. Measured separation distances obtained from blast wave detections in a single location are within 0.5% of the reference value measured through the beam profiler. This procedure is therefore a practical and reliable alternative to the measurement using beam profiler imaging, with similar quality. Its advantages concern associated costs, flexibility when measuring in constrained spaces such as in proximity to walls, and applicability to systems in which beam imaging is not an option, such as multi-point line FLDI.

1 Introduction

Focused Laser Differential Interferometry (FLDI) is a non-invasive measurement technique capable of detecting flowfield density fluctuations with remarkable spatial and temporal resolution, being especially suited to the field of experimental hypersonics (Parziale et al. 2013). With simple modifications, it is also possible to use FLDI as a velocity measurement tool by producing two closely spaced probing volumes to obtain a double-foci FLDI (D-FLDI), as shown by Jewell et al. (2016). The detected signal using the two probing volumes is very similar but for a time lag, which can be converted into convection speed measurement if the distance that separates the two systems is known.

In the precursor exploration by Jewell et al. (2016), velocity estimates of second-mode instability wavepackets in a hypersonic boundary layer consistent with typically expected values were obtained using D-FLDI. Exploratory work on velocimetry by means of parallel FLDI measurements has since then been conducted in multiple laboratories. Jewell et al. (2019) presented velocity measurements of compressible turbulent jets. Results followed the jet nominal values, albeit with a consistent offset. Ceruzzi and Cadou (2019) also performed velocity measurements of a turbulent free jet of air. Results agreed to hot-wire measurements and a velocity decay model if a certain distance from the jet exit was observed, although large uncertainties were reported. Bathel et al. (2020) used a carefully adjusted D-FLDI with parallel optical axes to probe a laser-induced breakdown shock wave and a conical hypersonic boundary layer with second-mode instabilities. Measured shock wave convection velocity was in close agreement to the reference obtained from simultaneous high-speed schlieren, and with lower uncertainty. Reasonable agreement was also verified for the velocity of the instability wavepackets, for which FLDI and high-speed

✉ Giannino Ponchio Camillo
  Giannino.PonchioCamillo@dlr.de

  Alexander Wagner
  Alexander.Wagner@dlr.de

1 German Aerospace Center (DLR), Institute of Aerodynamics and Flow Technology, Göttingen, Germany

schlieren were performed in different runs of the shock tunnel. Weisberger et al. (2020) presented FLDI velocimetry using a novel type of arrangement, in which a multi-point line FLDI is obtained. Convection velocity of laser-induced breakdown shock waves were reported with close agreement to high-speed schlieren measurements. Another novel methodology to obtain an array of FLDIs was used in Gragston et al. (2021b) to detect second-mode instabilities in the boundary layer on a flared cone. The obtained wavepacket convection velocities were within the expected range with respect to the nominal boundary layer edge velocity.

The accuracy and precision of velocimetry by means of double- or multi-foci FLDI depend on two main parameters. First, how well the two signals correlate, since the agreement between them informs the time lag to the velocity calculation. This depends on what proportion of the flowfield structures detected with the upstream system convect with little or no change until the downstream one. By taking into account the length scales of the probed flowfield, the distance separating the FLDI systems can be adjusted accordingly to improve signal agreement. The second parameter is how this distance is measured, as the quality of the obtained value is directly transferred to the velocity estimation. This was highlighted by Weisberger et al. (2020) concerning their measurements using adjacent channels of a multi-point line FLDI array, which yielded uncertainties in the order of ±10%. In that same work measurements with ±0.9% uncertainty were reported when using channels from separate lines, the difference being only how the spacing between the FLDI probes was determined. A similar occurrence is also seen in Ceruzzi and Cadou (2019) with the turbulent jet measurements, in which the separation between probes in the D-FLDI was given with ±6% and the velocity measurements presented large error bars.

Three methods are currently established in the literature to obtain the separation distance between FLDI systems: directly imaging the beams with a beam profiler; gradually blocking the beams with a precision-controlled stopper (Weisberger et al. 2020); or analyzing the system response to a lens with large focal length crossing the path of the beams (Ceruzzi and Cadou 2019).

The beam profiler offers a direct and precise measurement, but is not applicable if the systems are not physically discrete, such as the line FLDI. Additionally, it may not be available in all laboratories due to its significant cost in comparison with common FLDI components. The beam-blocking approach also requires specific precision equipment, and was shown to present unsatisfactory precision. The lens response method is inexpensive, but time-consuming and also subject to higher uncertainties as will be further detailed in this work. Furthermore, the beam profiler and the lens methods rely on the existence of certain spatial clearance to accommodate either instrument dimensions or

their movement, which may prevent their application when the FLDI beams are positioned close to a surface, e.g., for boundary layer measurements. These difficulties are minor if beam separation measurements are performed in the preparation phase of an experimental campaign, with flexible time and physical constraints. However, the FLDI has a number of flexible parameters (positioning, differentiation axis, sensitivity, beam convergence, to name a few) which may be tuned or changed in the course of the experiments, as exemplified in Weisberger et al. (2020) and Siddiqui et al. (2021). Such adjustments require choosing and manipulating optical components, which may change the separation distance of the FLDI systems. An updated distance measurement is therefore required, in which the disadvantages of these methods may become relevant.

The present work introduces an alternative approach to measuring the separation distance between FLDI probes, while addressing the limitations pertaining to the current methodologies. The procedure is based on the detection of a propagating weak blast wave, generated with an electric spark in ambient air. The practical advantages analyzed in the present study and the preference for low-cost equipment of easy access are meant to render this technique easily applicable in other laboratories. The developments presented in the next sections are constrained to a double-foci FLDI, but can be directly extrapolated to arrays of more foci, regardless of whether they are optically discrete or continuous on the focal plane.

2 Theoretical background

2.1 Indirect estimation of FLDI parameters

Two parameters pertaining to FLDI diagnostics are relevant in this work. Namely, the small distance separating the two foci which make one FLDI, and the greater distance that separates two independent FLDI systems. For convenience, the former will be referred to as internal or Δx_1 and the latter, external or Δx_2. Figure 1 shows a schematic of the FLDI used in this work and illustrates these distances. Accurate knowledge of the internal separation distance is necessary to correctly interpret the FLDI data, given its differential nature. The external separation is in turn useful when using multiple FLDI bundles to measure convection velocities by means of data cross-correlation.

Approaches to indirectly estimate these distances are valuable when the beams cannot be directly imaged with a beam profiler, e.g., due to hardware or spatial constraints. One such method is presented in Fulghum (2014) to obtain Δx_1 by analyzing the FLDI response to a weak lens crossing its path along the axis of beam separation. The method
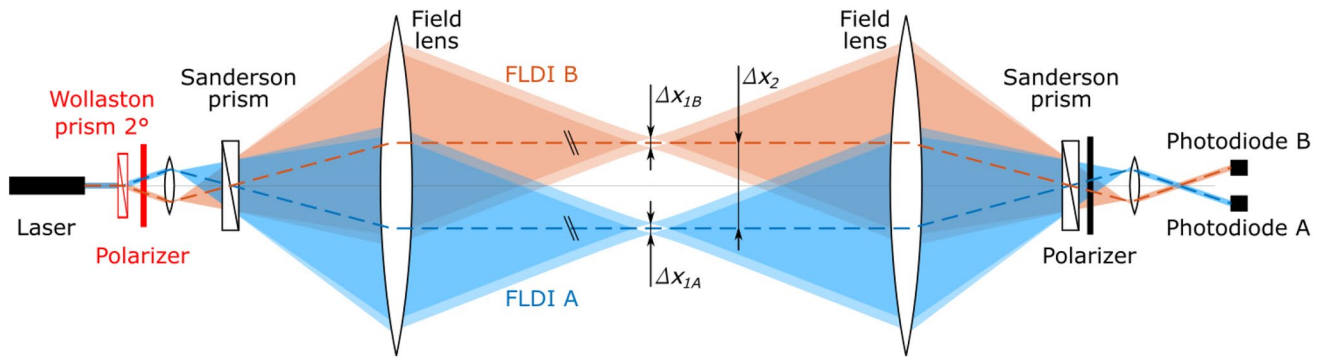
Fig. 1 Schematic of a double-foci FLDI system with constant separation distance. Beams propagate from left (pitch-side) to right (catch-side). The two independent FLDIs are shown as different colors. Optical components required to duplicate the standard system are highlighted in red

was later extended to also obtain Δx_2 in Ceruzzi and Cadou (2019).

The procedure consists of registering the D-FLDI output as a lens of long focal length (in the order of meters) is moved along the axis of beam separation. The output of each FLDI will describe a sinusoid when plotted as a function of the displacement of the lens. The period of the sinusoid depends on Δx_1 and the focal length of the lens. The size and focal length of the lens can hence be chosen such as to provide at least one full sinusoid period when traversed across the path of the FLDI beams. With the D-FLDI, the sinusoids produced by each FLDI will be out of phase, due to the distance between them Δx_2 as the moving lens is probed. The mathematical description of this behavior is summarized below in view of clarifying the terminology and relevant parameters for the present work.

If the FLDI response to the moving lens is normalized to have unitary amplitude, the corresponding sine wave when the lens moves along the x-axis can be described as:

$$y_n = \sin\left(\frac{2\pi}{T_n}x + \varphi_n\right) \tag{1}$$

with T_n and φ_n denoting the spatial period and the phase respectively, and $n = A, B$ representing the two FLDIs. The dependence of T_n and φ_n with Δx_1 and Δx_2 is given by:

$$\Delta x_{1n} = \frac{\lambda_0 f_L}{T_n} \tag{2a}$$

$$\Delta x_2 = \frac{\bar{T}}{2\pi}(\varphi_A - \varphi_B) \tag{2b}$$

with f_L denoting the focal length of the weak lens and an average period $\bar{T}$ employed to calculate Δx_2. This is a reasonable approximation because the two periods T_A and T_B are ideally identical, since in the type of D-FLDI configuration used here the optical piece controlling Δx_1 is shared by the two FLDIs. An alternative to this approximation is to

cross-correlate the two sinusoids to find the spatial lag between them. However, a limited sample of sinusoid cycles resulting from the movement range of the lens can lead to considerable inaccuracy on the spatial lag estimation. The results in this work were obtained using Eq. (2b) to calculate Δx_2.

Another indirect approach to estimate Δx_1 concerns the geometric disposition of the FLDI components. As detailed in Sect. 3.1, the internal separation distance originates from a divergence angle ε introduced in the FLDI beam at the focus of its field lens f_L on the emitting side. Assuming small angles, geometric optics yield simply $\Delta x_1 = f_L \varepsilon$. In this work, the divergence angle is produced by means of a Sanderson prism (Sanderson 2005), which consists of a bend-stressed polycarbonate bar. Following the approach in Biss et al. (2008), linear elastic theory can be used in combination with the properties of the prism material to estimate the resulting divergence angle introduced between the beams:

$$\varepsilon = \frac{\lambda}{f_\sigma}\frac{6E\delta b}{(Y^2 - 3L^2)} \tag{3}$$

with E the material modulus of elasticity, δ the bending deflection, b the thickness of the bar and Y and L describing the bending supports as shown in Fig. 2. The fringe-stress coefficient f_σ is an optical property of the polycarbonate material measured using a light source of wavelength λ, with their ratio remaining constant for varying wavelengths.
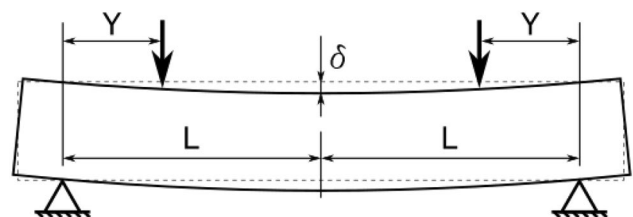

Fig. 2 Schematic of the arrangement to generate a pure bending moment

2.2 Blast waves

A blast wave is originated in a fluid as a result of sudden movement, such as the expansion of high-pressure gases previously confined, or an instantaneous localized energy release. The pressure disturbance caused by such an event propagates away from its source with the local speed of sound. In ambient air, the elevated pressure is accompanied by an elevated temperature, which causes the local speed of sound to increase. With these portions of the disturbance propagating faster than their vicinity, a discontinuity is eventually formed as a shock wave front (Kinney and Graham 1985).

The velocity described by a moving shock wave is proportional to its strength. In the case of blast waves originated by localized events such as energy addition in a finite volume, the strength of the shock wave front will progressively become weaker due to volume divergence, dissipation and relaxation. As the blast wave loses strength, it eventually becomes an acoustic pulse, propagating approximately with the ambient sound speed. Even in this limit, it still retains a distinct pressure signature marked by a compression phase and an expansion phase. This waveform of unique shape and known convection speed offers ideal conditions for the experimental detection of distances. Nonetheless, this requires knowing at which point the blast wave is adequately approximated as an acoustic pulse.

An accurate physical simulation of the blast wave evolution is beyond the scope of this work. Instead, a simple formulation of blast wave convection velocity as a function of distance is pertinent. Specifically, the case of very weak blast waves, with $M \approx 1$ no more than a few centimeters from the source will be of interest.

Jones et al. (1968) proposed a simple theoretical model to estimate the trajectory of the blast wave generated by a lightning discharge. The model is based on the strong shock similarity solution for a cylindrical shock wave, first-order corrected for the weak shock limit[1]. It will be shown in Sect. 4.2 that for the spark-generated disturbance in this work, the region with significant gradient of blast wave propagation velocity is confined to the vicinity of the source (distances of same order of magnitude as the length of the

spark). Therefore, assuming the shock wave to be cylindrical is reasonable when considering the blast wave trajectory estimation.

The trajectory of the shock wave front is described in terms of radius R and arrival time t. The undisturbed speed of sound c_0 and a characteristic radius R_0 are used to nondimensionalize R and t as $x = R/R_0$ and $\tau = c_0 t/R_0$, respectively. The characteristic radius is defined as:

$$R_0 = \sqrt{\frac{4E_0}{\gamma B P_0}} \tag{4}$$

with γ the specific heat ratio (assumed constant), P_0 the undisturbed ambient pressure, E_0 the energy deposited per unit length and $B = 3.94$ a constant for air. The trajectory for the weak shock is described as:

$$\tau = \frac{1}{2}\left(\sqrt{1 + 4x^2} - 1\right) \tag{5}$$

Equation (5) can be used to obtain an analytic expression for the dimensional shock wave convection velocity $U_s = dR/dt$ as a function of the distance to the blast wave source R, as:

$$U_s = c_0 \frac{\sqrt{1 + 4(R/R_0)^2}}{2R/R_0} \tag{6}$$

In this equation, the only unknown parameter is R_0, which is determined by the energy addition E_0 following Eq. (4). An experimental method to obtain E_0 will be shown in Sect. 4.2.

3 Experimental setup

3.1 Double-foci FLDI

The D-FLDI arrangement used in this work is shown schematically in Fig. 1. The laser source is a 200 mW Oxxius LCX-532S DPSS laser with nominal wavelength 532.3 nm. As mentioned in Sect. 2.1, Sanderson prisms are used to split the beams into interferometric pairs. The prismatic bar is a 6 mm thick Makrolon® bent with $L = 85$ mm and $Y = 29$ mm (refer to Fig. 2). Light intensity after beam recombination is measured using Thorlabs DET36A2 photodetectors, terminated with 50Ω. The outputs from the photodiodes were amplified 25 times using a SRS SR445A DC-350 MHz preamplifier. All data presented in this work were recorded for 1 ms using an AMOtronics transient recorder with DC-coupling and a sampling rate of 100 MHz.

The FLDI presented here has been designed to operate in the HEG shock tunnel (DLR 2018). The free gap between the field lenses is approximately 3.8 m. The beams are expanded to approximately 45 mm diameter at the field

---

[1] Bach and Lee (1970) proposed a more complex model, derived from the Navier–Stokes equations assuming a power law for the density profile behind the shock wave. Although this is not the case for the weak shock limit, the authors highlight that the obtained shock trajectory would remain accurate in the limit due to the conservation of total mass and energy. The solution obtained through this method has been compared to the one from the approach of Jones et al. (1968), yielding identical results for trajectory. For simplicity, the approach from Jones et al. (1968) is retained in this work.

Table 1 Sanderson prism deflections (measured) and corresponding beam divergence angles (estimated from linear elastic theory) investigated in the present work, separated by method and scope

Method	Scope	δ [mm]	ε [arc min]
Beam profiler	$\Delta x_1, \Delta x_2$	0.25, 0.40, 0.55, 0.70, 0.90, 1.10, 1.40	0.42, 0.58, 0.75, 0.92, 1.14, 1.36, 1.69
Moving lens	$\Delta x_1, \Delta x_2$	0.30, 0.59, 0.95, 1.45	0.47, 0.79, 1.19, 1.75
Blast wave	Δx_2	0.30, 0.59, 0.95, 1.45	0.47, 0.79, 1.19, 1.75
Linear elastic theory	Δx_1	0.00 to 1.80 (continuous)	0.14 to 2.14

lenses, which have a diameter of 100 mm and focal length 500 mm.

Eleven different values of Sanderson prism deflection were used, allowing flexibility of separation between the orthogonally polarized components in the range of $70 \le \Delta x_1 \le 250 \, \mu m$. When adjusting the prism deflection, bending was always applied past the intended value and then returned to it, to avoid hysteresis following Biss et al. (2008). The prism deflections δ were measured with a deflection gauge with 0.01 mm precision. The investigations were separated into indirect evaluation using a lens with focal length 3 m and the present blast wave method (4 points), and direct measurement using a DataRay TaperCamD-UCD23 beam profiler (7 points) as detailed in Table 1. The table also shows the beam divergence angles corresponding to the Sanderson prism deflection values, for reference. These angles are estimates from linear elastic theory, including a vertical offset due to residual stress to be seen in Sect. 4.1.

Prior to blast wave measurements, the undisturbed response of the FLDI was adjusted to approximately halfway between its lowest and highest output, where sensitivity is at its maximum. This was accomplished by fine adjustment of the relative position of the Sanderson prism on the catch-side along the axis of beam separation. When the beam-splitting optics is manipulated in this way, the phase difference between the resulting colinear beams changes. Since the interferometer is adjusted to an infinite fringe configuration, this results in an uniform intensity change after the beams are made to interfere with the polarizer before the photodiode. This approach is present in Lawson et al. (2019), only using Wollaston prisms instead of Sanderson. Conversion of voltage produced by the photodetectors into phase difference was also performed following that work.

Duplication of the basic FLDI into two or more closely spaced systems can be achieved in many different ways (Ceruzzi and Cadou 2019; Jewell et al. 2019; Bathel et al. 2020; Weisberger et al. 2020; Gragston et al. 2021a). In the present work, the D-FLDI is produced by means of a Wollaston prism of 2° splitting angle together with a polarizer, highlighted in red in Fig. 1. In this approach, the prism splits the incoming beam into two diverging beams with orthogonal polarization. The accompanying polarizer is oriented to project the beams back into the original polarization plane, such that the remainder of the system operates identically to the single FLDI arrangement. With both the original beam and the polarizer oriented at 45° with respect to the fast axis of the prism, two systems with identical power are obtained.

The duplicated system is obtained regardless of the precise positioning of the pair prism-polarizer on the pitch-side, as long as it is placed before the pitch-side Sanderson prism. Depending on its position with respect to the expanding and field lenses on the pitch-side and their focal lengths, multiple values of bundle separation Δx_2 at the D-FLDI center plane can be achieved with the same Wollaston prism, which can be advantageous in investigations aiming at, e.g., comparing spectral amplitudes between multiple points. A novel approach following this objective with a grid of FLDIs is presented in Gragston et al. (2021a).

However, this flexibility comes at the cost of allowing the two FLDI systems to describe non-parallel trajectories between the field lenses, as their axes will cross either before or after the focal length of the pitch-side field lens for all but one specific position of the splitting prism-polarizer pair. This way, the separation between the systems Δx_2 will vary along the probing region, which must be considered when using the duplicated FLDI setup to perform flowfield velocity measurements. Since the signal obtained on each FLDI is an integration of flowfield disturbances across the probing volume, disturbances crossing the FLDIs at stations with different values of Δx_2 may bias the velocity measurement.

To avoid this, a parallel disposition of FLDI bundles is recommended in velocimetry applications, as highlighted in Bathel et al. (2020). In that work, a Nomarski prism was used to ensure parallelism between the FLDIs. This type of birefringent prism works similarly to the Wollaston prism used here, but redirects the output beams so that they cross at a point ahead of it. Parallelism between the two FLDIs is thus achieved by adjusting this crossing point to be at the focal length of the pitch-side field lens, i.e., to coincide with the Sanderson prism on the left in Fig. 1.

In the present work, a similar effect is achieved by combining the Wollaston prism with the convergent lens responsible for expanding the beams in the FLDI on the pitch-side. The precise position and focal length of the expanding lens

are predefined by a combination of other parameters in the FLDI, namely the focal length of the field lens, the desired distance between the field lenses and the desired maximum beam diameter. Once this is set, the position of the Wollaston prism with respect to the expanding lens is determined using geometric optics such that the image of the origin of the two output beams coincides with the location of the pitch-side Sanderson prism in the setup. The center axes of each FLDI generated using this approach are shown in Fig. 1 as dashed lines with the corresponding colors.

For system design purposes, an initial estimate of the resulting Δx_2 as a function of the position of the optical elements and the splitting angle of the Wollaston prism can be obtained through trigonometric relations. Once all components are in place, a more precise measurement of the final Δx_2 such as the procedure proposed in this work is essential to minimize errors in the velocity measurements.

3.2 Blast wave generation

The FLDI Δx_2 measurement methodology proposed in this work requires a known and repeatable density disturbance to cross the optical axis of the FLDI systems. This is achieved in a simple manner through a spark in ambient air at rest. In contrast to past works which have successfully used laser-induced breakdown sparks to study the FLDI response (Parziale 2013; Bathel et al. 2020; Weisberger et al. 2020), an electric discharge is used here. The advantages for the purpose of the current work are high positioning flexibility with reduced cost and safety risks, while producing a blast wave with as little strength as possible with good repeatability.

The weak disturbance is preferred here because the convection velocity of an expanding blast wave varies as it propagates, but tends asymptotically to the ambient speed of sound, as seen in Sect. 2.2. The premise is to use the known value of this lower bound to obtain the separation between the FLDI bundles from the time lag between the signals. Therefore, it is advantageous that the blast wave is weak enough to degenerate into an acoustic pulse as close as possible to the source, hence minimizing the required physical space and the influence of external factors. Furthermore, the spark generation in ambient air without requiring any specific environmental conditioning is aimed at facilitating the application of the method. Only the ambient temperature is required to determine the local speed of sound.

The electric spark is obtained by means of an automotive spark plug. The distance between the electrodes of the spark plug is increased to approximately 4 mm such that the resulting blast wave produces the necessary amplitude of density fluctuations to be detected with the FLDI. A schlieren image of the spark-generated blast wave is shown in Fig. 3.

To study the evolution of the blast wave trajectory and determine the distance from the source beyond which the
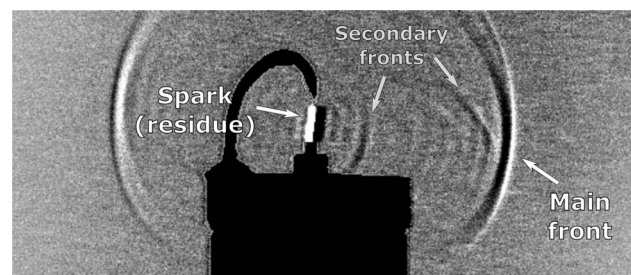

Fig. 3 Enhanced schlieren image of the blast wave generated using an automotive spark plug

propagation velocity is $M \approx 1$, the spark plug setup is installed on a translating mount with 0.1 mm precision. This allows the blast wave source to move along the axis of separation between the FLDI bundles, while the FLDI setup remains untouched. The combined uncertainty of operator and hardware to control this movement was estimated as ± 0.25 mm. The origin of the mount places the center of the gap between the electrodes approximately at the middle point between the two FLDIs. This was manually adjusted in a much coarser manner, with uncertainty in the order of 1 mm. Given the sensitivity of the theoretical velocity distribution to the origin of the blast wave, the vector of measurement positions is allowed to be uniformly offset by an optimization algorithm when processing the results, as will be detailed in the next section.

Measurements were taken at 23 positions corresponding to nominal distances between spark source and FLDI probe of 3 mm to 50 mm. The spacing between adjacent probing positions was made smaller closer to the source, where the velocity gradient is larger. The spark plug was controlled to produce a single spark during the recording time, allowing the disturbances to fully dissipate between discharges. Ten blast waves were generated and recorded at each position. The lowest and highest observed time lags were discarded, and the remaining 8 were individually analyzed. The ambient temperature near the probing region was measured with a digital ambient thermometer with precision of 0.05°C before each series of measurements to calculate the ambient sound speed. When the sound speed is used in Sect. 4.2 to determine Δx_2, the uncertainty carried over from the temperature measurement is less than 0.01% and will therefore be neglected.

4 Results and discussion

4.1 Estimation of distances with existing methods

An example of the results following the procedure described in Sect. 2.1 is shown in Fig. 4. The data were obtained
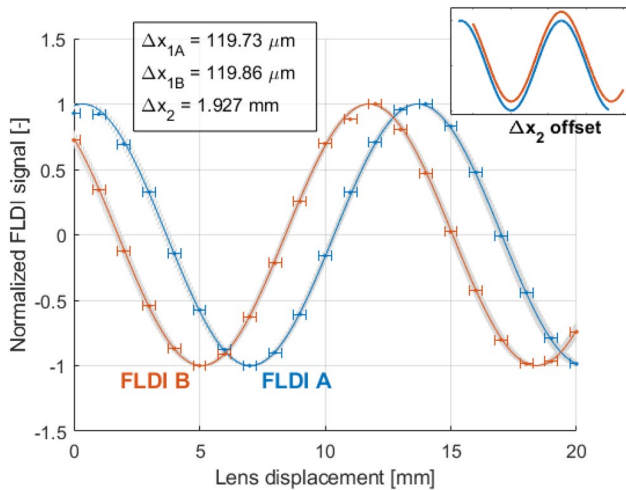
Fig. 4 Normalized double-foci FLDI response to a moving lens. Dots with error bars denote the acquired datapoints and lines correspond to least-square fits of sine functions. Shaded areas around the sinusoids are possible fits considering randomized errors along the lens displacement points. Resulting Δx_1 and Δx_2 measurements are displayed in the textbox. The inset shows the result of horizontally offsetting one of the sinusoids by Δx_2, ideally causing the two lines to overlap. They are also vertically offset by 10% for clarity. Data corresponding to Sanderson prism deflection $\delta = 0.59$ mm

using the D-FLDI described in Sect. 3.1 with Sanderson prism deflection $\delta = 0.59$ mm and a lens with focal length $f_L = 3$ m. The horizontal error bars correspond to the ± 0.25 mm combined uncertainty of operator and hardware to control the lens position, which was performed using the same supporting mount used for the spark generator described in Sect. 3.2.

The period and phase of the sine functions in the form of Eq. (1) are determined using least-squares method on the normalized FLDI output. A Monte Carlo approach is adopted to estimate a representative uncertainty for the fitted sinusoids as follows. Uniformly randomized errors on the lens displacement values within the assumed uncertainty of ± 0.25 mm are used to calculate 10,000 scenarios. The same modified lens displacement vector is used for both FLDIs in any given case, since the separation distance between them is constant and independent of this uncertainty. From the obtained distribution of periods and phases, an average sinusoid is obtained for each FLDI (blue and red lines in Fig. 4). An idea of the variation of the fits is given by the shaded area around each line, composed of 1000 different results from the Monte Carlo simulation. Values for Δx_1 and Δx_2 calculated using Eq. (2) with the average T_n and φ_n are shown in the textbox. Finally, the inset plot displays the two average sinusoids when one of them is offset in the x direction by the calculated Δx_2. An additional offset in the y direction is introduced for clarity, otherwise the lines are indistinguishable. The precise overlapping in terms of both
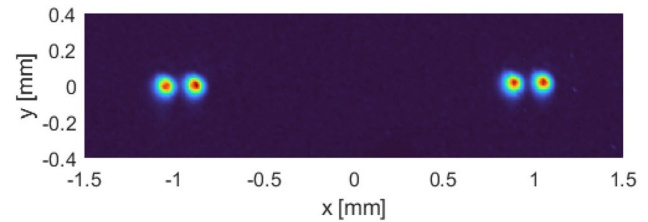

Fig. 5 Beam profiler image of the D-FLDI of the present work. Image obtained with Sanderson prism deflection $\delta = 0.9$ mm

phase and period is a validation of the physical assumptions of this methodology.

The distribution of period T_n and phase φ_n values obtained with the Monte Carlo approach are used to estimate the uncertainties for the calculated Δx_1 and Δx_2. Based on Eq. (2), the propagation of uncertainties σ of Δx_1 and Δx_2 given uncertainties for period T and phase difference $\Delta \varphi = \varphi_A - \varphi_B$ yields:

$$\sigma_{\Delta x_{1n}} = \frac{\lambda_0 f_L}{T_n^2} \sigma_{T_n} \tag{7a}$$

$$\sigma_{\Delta x_2} = \sqrt{\left(\frac{\Delta \varphi}{2\pi}\sigma_{\bar{T}}\right)^2 + \left(\frac{\bar{T}}{2\pi}\sigma_{\Delta \varphi}\right)^2} \tag{7b}$$

For the example shown in Fig. 4, Eq. (7) gives $\sigma_{\Delta x_{1A}} = 0.86~\mu m$, $\sigma_{\Delta x_{1B}} = 0.75~\mu m$ and $\sigma_{\Delta x_2} = 0.11$ mm. Hence the Δx_1 obtained for the two FLDIs shown in the textbox in Fig. 4 is the same within the uncertainty bounds, which is expected and validates the approach of using an average $\bar{T}$ in Eq. (2b). It is also noted that the uncertainty of Δx_2 is proportionally much larger than that of Δx_1. This is a consequence of the lens displacement uncertainty having a much greater influence on the phase of the sine wave than on its period, as can be inferred from the shaded regions in Fig. 4.

Complementary to the beam distance measurements performed with the moving lens, the FLDI beams were imaged at the center plane of the D-FLDI using a beam profiler. An example of the obtained image is given in Fig. 5, for Sanderson prism deflection $\delta = 0.9$ mm. The resolution of the beam profiler was in situ calibrated as 10.3 μm per pixel. Distances Δx_1 and Δx_2 were measured by detecting the peak values of profiles resulting from averaging the pixel intensities along each vertical line of the images. Ten independent images were obtained for each Sanderson prism deflection. To achieve sub-pixel accuracy, the average pixel intensity profile of each independent image was interpolated using a shape-preserving cubic interpolation and smoothed using a moving average. The pixel difference between the peaks identified in the resulting profiles was then converted to
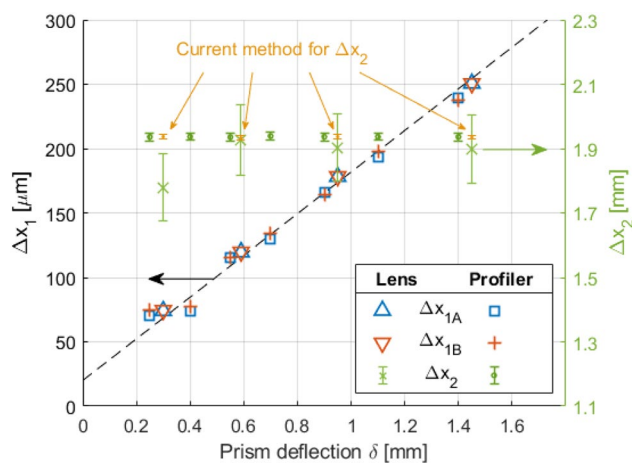
Fig. 6 Values for FLDI Δx_1 (left y-axis) and Δx_2 (right y-axis) measured using the moving lens method and beam profiler images for multiple adjustments of Sanderson prism deflection δ. The dashed line indicates the linear elastic theory prediction, vertically offset to best fit the data. The values for Δx_2 obtained with the method suggested in this work are also shown for comparison

distances and used to calculate a mean value and standard deviation.

By changing the deflection of the Sanderson prism δ and repeating the procedures described above, the dependency of Δx_1 with the prism deflection δ can be demonstrated. Figure 6 shows the results of this calibration for multiple values of δ, with Δx_1 plotted on the left y-axis and Δx_2 on the right one. The expected results are that Δx_1 linearly increases with the prism deflection δ, while Δx_2 remains unchanged since it is not defined by the Sanderson prism settings. The linear elastic theory estimate for Δx_1 is obtained from Eq. (3), using the optical properties for polycarbonate mentioned in Biss et al. (2008), namely $f_\sigma = 7.0$ kN/m for $\lambda = 546.1$ nm, and the mechanical properties of Makrolon® following the manufacturer datasheet, $E = 2.4$ GPa. A small vertical offset is introduced in the theoretical prediction to account for the trend of an apparent finite Δx_1 with $\delta = 0$. This may be due to a residual stress field in the prism, as highlighted in, e.g., Fulghum (2014) and Birch et al. (2020).

The results show that Δx_1 has a similar behavior for both FLDIs, with values that coincide for a given δ and which are well described by the correlation obtained using linear elastic theory once an empirical estimate of residual stress offset is taken into account. Uncertainties for Δx_{1A} and Δx_{1B} for both the lens and profiler methods have similar magnitude as presented for the example above (order of 1 μm), and are not plotted for clarity. A comparatively low accuracy of the beam profiler results is observed for the lower end of δ values. This is a result of inadequate pixel density of the instrument to detect beams this close together, making them harder to distinguish.

Regarding Δx_2, the distribution of values calculated through the moving lens method admits the definition of a horizontal line that crosses all points within their uncertainty. Such a line would confirm the expected behavior of Δx_2 not depending on the Sanderson prism configuration. However, a noticeable fluctuation among the calculated values of Δx_2 can be observed, even though they all yielded a similar good signal overlap as seen in the inset of Fig. 4 (not shown). Together with the relatively large error bar of each obtained value (approximately $\pm 6\%$), concern is warranted as the uncertainty in Δx_2 is directly fed through to the measurement of velocities using the D-FLDI. One way to lower this uncertainty is to collect more independent sinusoid sweeps, such as to obtain a reliable mean of Δx_2 with an associated standard deviation. Another way is to address the large uncertainty of each calculated Δx_2, by reducing the influence of the lens displacement uncertainty on the sinusoidal fits. This may be accomplished by either reducing the uncertainty of each point (e.g., with careful operator action) or by using more points on each sweep. All these alternatives, however, significantly add effort to a procedure that is already inherently time-demanding.

Looking at the Δx_2 estimates from the beam profiler images, a much more consistent distribution is observed. The uncertainty of each point is significantly smaller than the moving lens results, at $\pm 0.6\%$. Also, the mean values remain unchanged for different values of Sanderson prism deflection, with a mean of $\Delta x_2 = 1.937 \pm 0.001$ mm. For a direct comparison, the results obtained with the method presented in this work are also highlighted in Fig. 6. Excellent agreement to the beam profiler results can be verified. The details pertaining to these measurements are presented in the next section.

4.2 Estimation of distances through blast wave detection

An alternative to the procedures exemplified in Sect. 4.1 is presented in this section. A blast wave is used as a means to produce a disturbance with clear signature on the FLDI response. The main objective here is to measure Δx_2 with low effort and increased precision, addressing the issues highlighted previously.

A sample of blast wave detection using D-FLDI is shown in Fig. 7. For ease of operation in the experimental setup, FLDI B is upstream of FLDI A with respect to the blast wave source, but equivalent results may be obtained inverting the disposition of source and probe. The D-FLDI response is minimally post-processed to values of phase difference $\Delta\Phi$. The time axis is arbitrarily offset to yield $t = 0$ when the blast wave arrives at FLDI B, since the method explored in this section is independent of the blast wave travel time upstream of the first FLDI bundle. The clear shape described
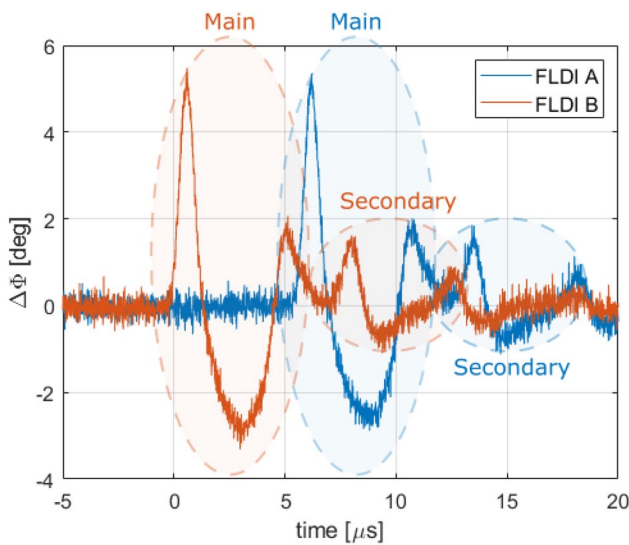
Fig. 7 Blast wave detection using the double-foci FLDI. Spark generator is 30 *mm* from FLDI B, which is upstream of FLDI A. Main and secondary events are highlighted. The origin of the time axis is arbitrarily offset to match the blast wave arrival at the position of FLDI B. Data corresponding to Sanderson prism deflection $\delta = 0.95$ *mm*

by the blast wave detection on each FLDI indicates that an accurate estimate of time lag can be obtained as a peak in the cross-correlation between the signals.

It is also noteworthy that the signal detected with each FLDI is almost identical but for the time lag. This is expected since the blast wave does not undergo significant changes between the closely spaced FLDI probes, unless very close to the spark source. Nonetheless, the multiplication of FLDI beams requires the addition of system components and complexity. The quality and sensitivity of the resulting double- or multi-foci FLDI may not be identical, and hard to quantify. The controlled disturbance produced with the electric spark may therefore be used as a reference to identify potential issues that may need addressing.

In Fig. 7, secondary events are observed in the time signals occurring after the passage of the main blast wave. These events correspond to interactions between the blast wave and the spark plug structure, as can also be seen in the schlieren image of Fig. 3. Events of this nature were verified to have been strong enough at certain stations to bias the cross-correlation of the signals if included. Nonetheless, they were always sufficiently separate from the main blast wave signature to be easily discarded from the signals prior to cross-correlation, hence not interfering with the results presented here.

It should be noted that cross-correlating the signals to obtain the time lags is preferred for robustness. By taking into account the full signature of the blast wave on the FLDI probes, the lag measurement becomes less sensitive to eventual flowfield non-uniformities or signal-to-noise-ratio

issues. Nonetheless, time lags may also be obtained with simpler approaches, such as measuring the time difference between the signal peaks. This is an alternative if the signature from the blast wave is not as easily isolated from secondary events as shown here. An example is if the FLDI probes are positioned with respect to the surface of a model at a certain distance which is not large enough to allow the reflected wave to arrive significantly later than the main one, nor small enough for the main and reflected wavefronts to merge together before reaching the FLDI probes (Kinney and Graham 1985).

Since the blast wave propagates with increased speed near the source and the D-FLDI is kept unchanged, the obtained time lags increase as the source is moved away from the D-FLDI. When the time lags stabilize around a certain value, an indication is obtained that the acoustic limit of the blast wave was reached, in which it propagates with $M \approx 1$. For a more accurate prediction of this region, Eq. (6) is used to obtain the analytic distribution of wave convection velocity. In this equation, a single unknown determines the trajectory of the wavefront, namely the energy deposited by the spark E_0, which defines R_0 through Eq. (4). Since the distance between the two FLDIs is the same for all blast wave probings, the spark energy can be obtained using the detected distribution of time lags without explicit knowledge of the distance Δx_2, as the solution for an optimization problem as follows.

In a D-FLDI constructed as presented in this work and considering the very weak blast wave produced, the velocity gradient between the two FLDI bundles will generally be small enough to be neglected without incurring an excessive error. This way, at each probing location R_i (measured with respect to the blast wave source) the distance Δx_2 will be given as a function of the time lag Δt_i as $\Delta x_2 = U_s(R_i) \cdot \Delta t_i$, with the blast wave velocity U_s a function of R_i (and E_0) according to Eq. (6).

Because Δx_2 is kept constant as the blast wave source is moved away, the product between the theoretical U_s and the experimental Δt must remain constant for all measurement locations $i = 1, \ldots, n$ when the correct value of E_0 is used. In other words, the derivative of $U_s(R_i) \cdot \Delta t_i$ with respect to the radial coordinate r must be zero. The numerical optimization problem hence becomes finding E_0 that minimizes the objective function f composed by the quadratic sum of these derivatives:

$$f(E_0) = \sum_{i=1}^{n} \left[\frac{d}{dr} \left(U_s(R_i) \cdot \bar{\Delta} t_i \right) \right]^2 \qquad (8)$$

The derivative in each point R_i is roughly approximated through the mean value theorem, by means of finite differences between R_{i-1} and R_{i+1}. This is a reasonable approach because the distribution of velocities and time lags along

the radial coordinate is expected to describe a well-behaved function. This is further conditioned by using for each location the average of time lags obtained with the independent measurements, denoted above with the bar over Δt_i.

As mentioned in Sect. 3.2, the origin of the position vector was manually adjusted to roughly place the spark generator at the middle point between the two FLDIs. However, the theoretical velocity distribution Eq. (6) is highly sensitive to the accuracy of this origin to adequately capture the region of stronger velocity gradients. Therefore, a second optimization layer was introduced in the algorithm, allowing a systematic offset of the position vector to be adjusted. This layer was placed above Eq. (8), searching for the value of position vector offset which minimized the standard deviation of the distances calculated as $U_s(R_i) \cdot \bar{\Delta} t_i$ resulting from the inner optimization layer. This target is sustained by considering that the perfect representation of the data by the theoretical curve should yield the exact same Δx_2 on all points. A schematic representation of the full algorithm is shown in Fig. 8. Although this double-layer procedure yields a noticeable improvement on the overlapping of experimental data and theoretical model, adequate results can also be obtained without the second (outer) optimization layer, with the resulting Δx_2 having been observed to vary by a maximum of only 0.7%.

Once a value of energy deposition E_0 is found, the blast wave velocity as a function of its radius is determined. An estimate of the separation distance between the FLDI bundles Δx_2 can hence be obtained from any of the query points using the local velocity and the measured time lag. To demonstrate the method and provide an idea of precision, the values of Δx_2 reported here are obtained as an average between all points collected for each Sanderson prism configuration:

$$\Delta x_2 = \frac{1}{n \cdot m} \sum_{i=1}^{n} \sum_{j=1}^{m} \left(U_s(R_i) \cdot \Delta t_{i,j} \right) \tag{9}$$

where $i = 1, \ldots, n$ denotes the measurement positions as before, and $j = 1, \ldots, m$ represents the individual measurements performed at each position. With a total number of 184 independent measurements in each series ($n = 23$ positions, $m = 8$ measurements at each position), the standard deviation of the Δx_2 values is used as an estimate of uncertainty.

An example of the measurements and resulting calculated blast wave trajectory is shown in Fig. 9. The solid line represents Eq. (6) calculated using E_0 obtained from minimizing Eq. (8). The dots with error bars are the means and standard deviations of Mach numbers calculated using the experimental time lags and the separation distance Δx_2 calculated with Eq. (9). The horizontal error bars indicate the $\pm 0.25\ mm$ position uncertainty mentioned in Sect. 3.2.
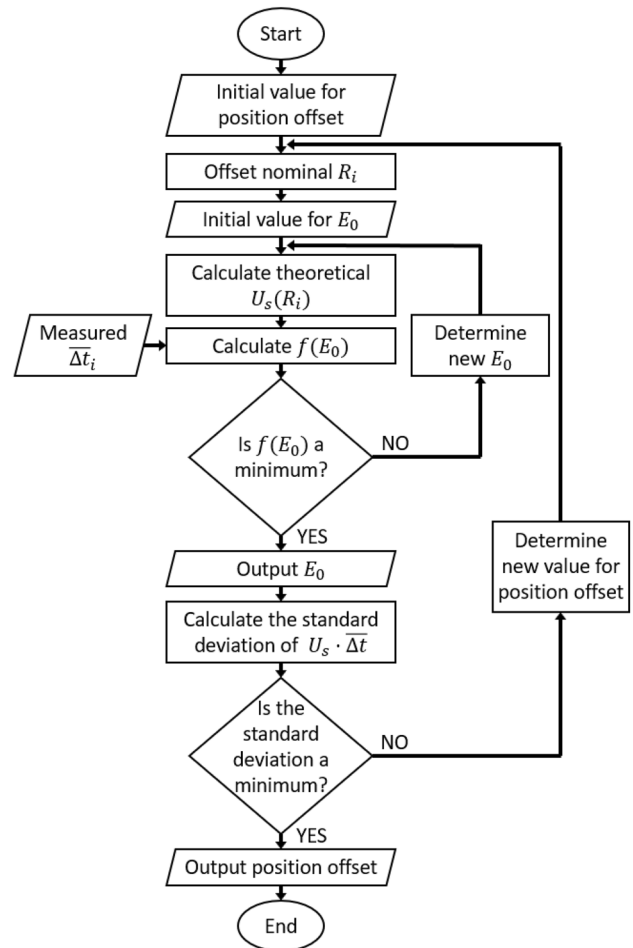

Fig. 8 Fluxogram of the double-layered algorithm to calculate the best theoretical fit to the experimental data. The $f(E_0)$ used in the inner layer is defined by Eq. (8)

The dotted lines in Fig. 9 are the blast wave trajectories obtained with variation of $\pm 30\%$ on the calculated E_0. The small influence of such a large difference shows that the accuracy of the energy deposition estimate is not a determinant factor for the D-FLDI parameter estimation studied here.

This procedure was repeated for the same Sanderson prism configurations used with the moving lens method. The obtained values of Δx_2 are reported in Table 2. Two important results can be highlighted in this table. First, the obtained values for Δx_2 are essentially the same across all different δ (hence Δx_1) as they should, and all agree with the beam profiler measurements to within 0.2% (refer to Fig. 6). Second, the standard deviation in all cases corresponds to less than 0.5% of Δx_2, i.e., a very consistent value of Δx_2 is obtained across all measurement points. Hence a precise measurement of Δx_2 can be performed by using time lags detected in a single position, as long as the blast wave local convection velocity is known.
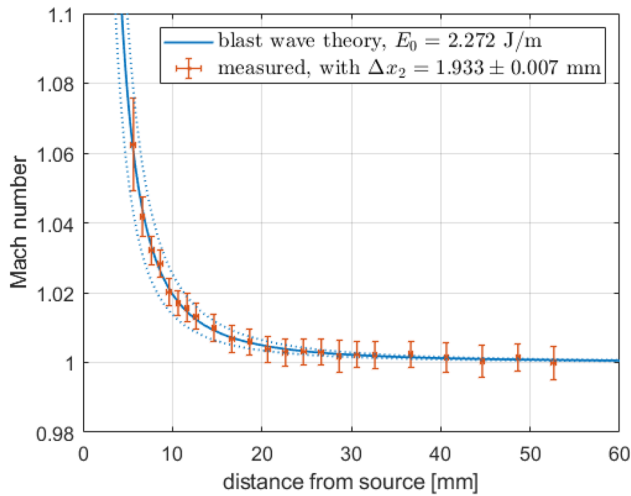
Fig. 9 Blast wave trajectory regressed from FLDI measurements. Solid line indicates the analytic solution using the E_0 value obtained from the optimization procedure. Dotted lines indicate the solutions for $\pm 30\%$ on the nominal E_0. Measured Mach numbers obtained from the time lags detected with D-FLDI, considering the separation distance indicated in the legend. Data corresponding to Sanderson prism deflection $\delta = 0.59$ mm

Table 2 Measured FLDI beam separation distances Δx_2 for different Sanderson prism deflections δ

Sanderson prism δ	Double-foci FLDI Δx_2
0.30	1.937 ± 0.008
0.59	1.933 ± 0.007
0.95	1.937 ± 0.006
1.45	1.935 ± 0.004
	Mean: 1.936

All units in *mm*

An adequate estimate of the velocity in the vicinity of the blast wave source can only be obtained with measurements at multiple locations, e.g., by means of the optimization procedure described here. Nonetheless, Fig. 9 shows that such an elaborate estimate is not strictly necessary. The sonic limit beyond which $M \approx 1$ is reached still relatively close to the source, for the case investigated here in which an automotive spark plug is the source of the blast wave. Farther than approximately 20 mm from the source, the blast wave convection velocity can be approximated as $M = 1$, requiring no further measurements. Processing in this simplified way the collection of measurements used to obtain Table 2 yielded no more than 0.5% difference to the beam profiler mean measurement, with standard deviations ranging from 0.2% to 0.7% in the upper limit of 95% confidence interval. Even if the experimental constraints force a measurement very close to the source, Fig. 9 indicates that

assuming $M = 1$ to calculate the beam separation distance from the signal time lags introduces no more than 3% error as close as 10 mm. Finally, if in addition to the approximation of $M = 1$, the time lags were obtained simply using the peaks of the signals instead of cross-correlation, as previously mentioned, the obtained differences to the beam profiler measurements were still 1% or less for distances to the spark source larger than 20 mm.

The method suggested here is therefore capable of providing a good experimental estimate of the beam separation distance Δx_2 of a double- or multi-foci FLDI with very low effort. The acquisition of repeated blast wave measurements at some location within the sonic limit region is quick and requires little mechanical preparation, with the whole process taking only a few minutes.

As a side note, the blast wave measurements can be further used to give an approximate estimate of the internal separation distance Δx_1 as follows. For any given distance from the source, the magnitude of the FLDI signal $\Delta\Phi$ will be proportional to the separation distance between the interferometric pair Δx_1. As long as this separation is kept small relative to the waveform of the blast wave, the ratio $\Delta\Phi/\Delta x_1$ is constant. It is an approximation of the spatial derivative of the disturbance, which remains unchanged between measurements if the source and the measurement location are the same. This way, if the separation $\Delta x_1|_{\delta_1}$ is known for one Sanderson prism deflection δ_1, the separation for other configurations δ_k, $k = 2, 3, \ldots$ can be obtained by matching the magnitude of the measured $\Delta\Phi|_{\delta_k}$, i.e., $\Delta x_1|_{\delta_k} = \Delta\Phi|_{\delta_k}/(\Delta\Phi/\Delta x_1)|_{\delta_1}$. However, at least one known value of Δx_1 is still required, and uncertainties are difficult to assess. Nonetheless, Fig. 4 in Sect. 4.1 has shown that linear elastic theory provides direct and reasonable estimates of this distance when a Sanderson prism is employed to produce Δx_1, requiring only a pre-strain offset to be adjusted. Once this is accomplished, it becomes a good practical substitute for the lens procedure if needed. The measurement of Δx_1 through blast wave detection is therefore only recommended for verification purposes.

5 Conclusion

The contributions presented in this work addressed a new methodology of indirect estimation of the distance separating the probing volumes of a double-foci FLDI, Δx_2. A weak blast wave generated in ambient air at rest using an automotive spark plug was shown to become an acoustic pulse close to its source. The known convection velocity of this type of disturbance, namely the ambient sound speed, was used to obtain Δx_2 from the time lag between the adjacent systems.

An analysis comprising a wide range of measurement locations showed that reliable and accurate estimates with

as little as $\pm0.4\%$ uncertainty (2σ) can be obtained from multiple measurements in a single location, which is easily and quickly executed. Comparison to direct measurements using a beam profiler showed differences smaller than 0.5% if a single location was used farther than 20 mm from the spark source, and less than 0.2% if multiple stations are combined. The measurements were shown to be consistent throughout multiple configurations of the FLDI Sanderson prism, which controlled the unrelated separation between the interferometric pair composing one FLDI, Δx_1.

The existing method of indirect assessment of beam separation distances using the FLDI response to a lens with large focal length was critically evaluated. Results corroborated its excellent ability to measure Δx_1. However, for Δx_2 the lens method yielded measurement uncertainties of $\pm6\%$, together with a considerable variation of the mean results (up to 5%) when Δx_1 was varied by means of Sanderson prism adjustment.

Velocimetry by means of FLDI measurements is only as accurate and reliable as the measurement of the separation distance between the FLDI systems Δx_2. The present method is therefore recommended as a means to obtain this value in double- or multi-foci FLDI. It preserves the low-cost benefit of the moving lens indirect approach while being much less time-consuming with improved accuracy and precision, both comparable to direct beam imaging. Additionally, it requires very little free space (20 mm length ideally, less if necessary), being more practical than a beam profiler in case of limited spatial availability such as in the proximity of model walls. Also, the non-imaging nature of this method makes it applicable to multi-point FLDI systems in which the foci are not optically separated.

Finally, it is worth noting that once the blast wave decays to an acoustic pulse, it propagates with little change between closely spaced FLDI probes. Being a simple, well-known and easily reproduced type of disturbance, it may therefore be a helpful reference for system response verification in multi-foci FLDI.

References

Bach GG, Lee JHS (1970) An Analytical Solution for Blast Waves. AIAA J 8(2):271–275. https://doi.org/10.2514/3.5655

Bathel BF, Weisberger JM, Herring GC, King RA, Jones SB, Kennedy RE, Laurence SJ (2020) Two-point, parallel-beam focused laser differential interferometry with a Nomarski prism. Appl Opt 59(2):244. https://doi.org/10.1364/ao.59.000244

Birch B, Buttsworth D, Zander F (2020) Measurements of freestream density fluctuations in a hypersonic wind tunnel. Exp Fluids 61:158. https://doi.org/10.1007/s00348-020-02992-w

Biss MM, Settles GS, Staymates ME, Sanderson SR (2008) Differential schlieren-interferometry with a simple adjustable Wollaston-like prism. Appl Opt 47(3):328. https://doi.org/10.1364/ao.47.000328

Ceruzzi A, Cadou CP (2019) Simultaneous Velocity and Density Gradient Measurements using Two-Point Focused Laser Differential Interferometry. In: AIAA Scitech 2019 Forum, American Institute of Aeronautics and Astronautics, https://doi.org/10.2514/6.2019-2295

DLR (2018) The High Enthalpy Shock Tunnel Göttingen of the German Aerospace Center (DLR). J Large-scale Res Facil 4:A133. https://doi.org/10.17815/jlsrf-4-168

Fulghum MR (2014) Turbulence measurements in high-speed wind tunnels using focusing laser differential interferometry. PhD thesis, The Pennsylvania State University

Gragston M, Price T, Davenport K, Zhang Z, Schmisseur JD (2021a) Linear array focused-laser differential interferometry for single-shot multi-point flow disturbance measurements. Opt Lett 46(1):154. https://doi.org/10.1364/ol.412495

Gragston M, Siddiqui F, Schmisseur JD (2021b) Detection of second-mode instabilities on a flared cone in Mach 6 quiet flow with linear array focused laser differential interferometry. Exp Fluids 62:81. https://doi.org/10.1007/s00348-021-03188-6

Jewell JS, Parziale NJ, Lam KL, Hagen BJ, Kimmel RL (2016) Disturbance and Phase Speed Measurements for Shock Tubes and Hypersonic Boundary-Layer Instability. In: 32nd AIAA Aerodynamic Measurement Technology and Ground Testing Conference, American Institute of Aeronautics and Astronautics, https://doi.org/10.2514/6.2016-3112

Jewell JS, Hameed A, Parziale NJ, Gogineni SP (2019) Disturbance Speed Measurements in a Circular Jet via Double Focused Laser Differential Interferometry. In: AIAA Scitech 2019 Forum, American Institute of Aeronautics and Astronautics, https://doi.org/10.2514/6.2019-2293

Jones DL, Goyer GG, Plooster MN (1968) Shock Wave from a Lightning Discharge. J Geophys Res 73(10):3121–3127. https://doi.org/10.1029/jb073i010p03121

Kinney GF, Graham KJ (1985) Explosive Shocks in Air. Springer, Berlin Heidelberg,. https://doi.org/10.1007/978-3-642-86682-1

Lawson JM, Neet MC, Grossman IJ, Austin JM (2019) Characterization of a Focused Laser Differential Interferometer. In: AIAA Scitech 2019 Forum, American Institute of Aeronautics and Astronautics, https://doi.org/10.2514/6.2019-2296

Parziale N (2013) Slender-Body Hypervelocity Boundary-Layer Instability. PhD thesis, California Institute of Technology

Parziale NJ, Shepherd JE, Hornung HG (2013) Differential Interferometric Measurement of Instability in a Hypervelocity Boundary Layer. AIAA J 51(3):750–754. https://doi.org/10.2514/1.J052013

Sanderson SR (2005) Simple, adjustable beam splitting element for differential interferometers based on photoelastic birefringence of a prismatic bar. Rev Sci Instrum 76(11):113703. https://doi.org/10.1063/1.2132271

Siddiqui F, Gragston M, Saric WS, Bowersox RDW (2021) Mack-mode instabilities on a cooled flared cone with discrete roughness elements at Mach 6. Exp Fluids 62:213. https://doi.org/10.1007/s00348-021-03304-6

Weisberger JM, Bathel BF, Herring GC, Buck GM, Jones SB, Cavone AA (2020) Multi-point line focused laser differential interferometer for high-speed flow fluctuation measurements. Appl Opt 59(35):11180. https://doi.org/10.1364/ao.411006